JPhys Photonics

ACCEPTED MANUSCRIPT • OPEN ACCESS

Manipulating optical absorption and polarization using microwave control in an atomic vapour

To cite this article before publication: Andrei Tretiakov *et al* 2024 *J. Phys. Photonics* in press https://doi.org/10.1088/2515-7647/ad2ac8

Manipulating optical absorption and polarization using microwave control in an atomic vapour

A. Tretiakov‡, C. A. Potts§, Y. Y. Lu‖, J. P. Davis & L. J. LeBlanc

Department of Physics, University of Alberta, Edmonton AB, Canada T6G 2E1

E-mail: lindsay.leblanc@ualberta.ca

Abstract. The multiplicity of atomic states (and the transitions between them) offer an innate, coherent platform through which microwave and optical fields effectively interact. In an atomic vapour near room temperature, we combine optical and microwave fields to generate a macroscopic internal angular momentum among the atoms – an atomic polarization – at an arbitrary angle with respect to the optical (laser) beam. This geometric freedom enables microwave control over photonic degrees of freedom, which we use in two demonstrations: using microwave-assisted optical pumping, we can rotate linear polarization through several degrees, and we can control the absorption for specific transitions and polarizations, which has applications for microwave-to-optical transduction.

1. Introduction

Atomic physics' vast array of techniques to exploit the light-matter interaction is used to control both the quantum states of matter, including fundamental studies such as in quantum many-body physics [1] and practical applications like precision timekeeping [2], and the quantum states of light, with examples ranging from generating squeezed states to preparing single-photon states for quantum communications. Even with the simple electronic structure of the alkali-metal atoms, the variety of transitions available within a single system is vast, offering extraordinary possibilities for coherently mediating electromagnetic signals across orders of magnitude in frequency.

In the realm of quantum technologies, interfaces between optical and microwave signals play an important role in connecting platforms performing complementary tasks [3]. Among the candidates for microwave-to-optical transduction, alkali-metal

‡ Present address: Department of Physics & Astronomy, University of California, Los Angeles, Los Angeles, CA, 90095, USA

§ Present address: Kavli Institute of NanoScience, Delft University of Technology, PO Box 5046, 2600 GA Delft, Netherlands

‖ Present address: Department of Electrical and Computer Engineering, University of California, Los Angeles, Los Angeles, CA, 90095, USA

atomic ensembles, which naturally support microwave and optical transitions, are promising in regimes of both quantum [4, 5, 6, 7, 8, 9] and classical signals [10, 11, 12, 13, 14, 15, 16, 17, 18, 19, 20]. These approaches to transduction are also attractive in that they facilitate the storage and retrieval of quantum information for quantum communications [21], with atomic systems among the best performing platforms [22, 23, 24]. In addition, the connections across frequency domains in atomic systems, using the nonlinear interaction between microwave and optical fields in alkali vapours, also enable applications like compact atomic clocks [25, 26, 27, 28, 29], microwave electrometry [30], and static and microwave magnetometry [31, 32, 33, 34, 35].

The atom-light interaction, mediated by the well-defined intrinsic angular momentum (or "spin") of atomic states, enables manipulation of the optical polarization with precise frequency selection. By controlling the external magnetic fields and polarized electromagnetic signals (for example, in microwave and optical domains) applied to the vapour, we can engineer both the *atomic polarization*, which is the particular configuration of atomic ensembles' quantum states, and the character of the light that emerges from the system. To access this level of control, multi-level atomic states with different spin configurations must be used. These principles are at the heart of applications including optically pumped atomic magnetometers [36, 37, 38, 39, 40], generating spin-polarized noble gases [41, 42], and atomic detection and imaging of electromagnetic fields [43, 44, 45]. Usually, the atomic polarization is parallel to the optical laser beam direction, but some approaches require the atomic polarization to be perpendicular to the probe laser beam [36, 38]; in an all-optical set-up, this is a non-trivial task that involves, for example, additional modulation of optical fields [46].

In this work, we introduce a novel technique for manipulating the absorption and polarization of optical fields through microwave control of an atomic ensemble of ^{87}Rb. We engineer the spin polarization in multi-state atomic ensembles based on microwave-assisted optical pumping (MAOP), which is similar to optically detected magnetic resonance (ODMR) methods in solid-state systems [47, 48], except here, we make use of configuration where at least one of the two ground-state levels includes several sublevels. MAOP results in atomic polarization that is determined by an external magnetic field vector rather than the orientation and polarization of the pumping laser beam, unlike optical pumping alone [49]. Here, we tailor the MAOP to generate microwave-induced optical birefringence and dichroism, which can be used to implement a polarization-selective microwave-to-optical interface, while the birefrengence leads to microwave-controlled nonlinear magneto-optical rotation [50] that can, for instance, be applied for signal transduction based on pulse carving [51].

2. Optical control via microwave-assisted optical pumping

Light incident on an atomic vapour is absorbed by atoms when it is resonant to a transition between available internal states, and when its polarization is compatible, according to the angular momenta of the states and the relevant selection rules. A

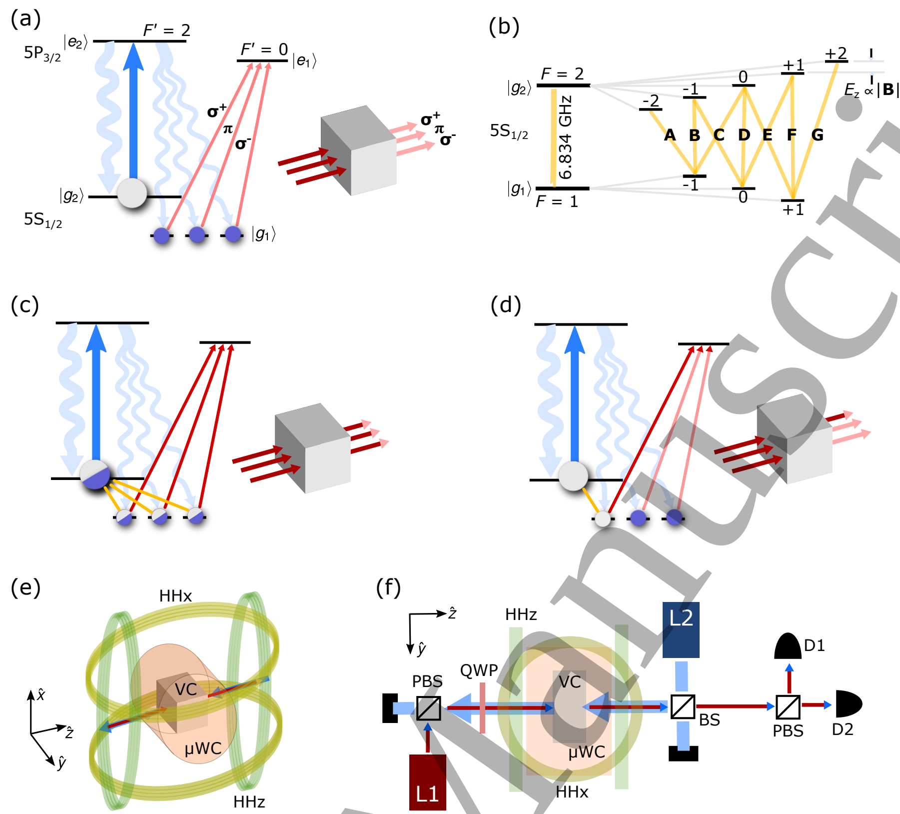

Figure 1. Experimental scheme for microwave-controlled optical absorption and magneto-optical rotation. (a) Atomic level scheme (for ^{87}Rb here, but generalizable to other atoms), including two ground states $|g_1\rangle$, $|g_2\rangle$. An optical transition (blue) connects this level $|g_2\rangle$ to excited state $|e_2\rangle$, from which spontaneous emission (wavy lines) repopulates both ground states. Weak probe beams (red) address the other ground $|g_1\rangle$ to excited $|e_1\rangle$ transition. Three separate lines are drawn indicating the three basis states for optical polarization. When the ground states are uncoupled, population accumulates in $|g_2\rangle$ and transmission of the probe through a vapour cell (right) is diminished. (b) Microwave transitions between Zeeman sublevels $|g_1\rangle = |F = 1\rangle$ and $|g_2\rangle = |F = 2\rangle$. Of the nine possible transitions, there are seven unique frequencies, labelled A-G. (c) As in (a), but a microwave field couples the ground states, reducing atomic population in $|g_1\rangle$, which increases the probe transmission through the vapour cell (right). (d) As in (c), but the microwave field is tuned to one sublevel of the $|g_1\rangle$ manifold, leading to microwave-assisted optical pumping to a subset of ground states. The absorption from this level thus depends on the polarization of light, leading to polarization-dependent controlled absorption. (e) View of vapour cell inside microwave cavity, surrounded by magnetic field coils. (f) Optical schematic. L1: probe laser; L2: pump laser; VC: vapour cell, HHx, HHz: Helmholtz coils along $\hat{x}$ and $\hat{z}$; (P)BS: (polarizing) beam splitter; D1/2: photodetectors; QWP: quarter-wave plate.

static magnetic field $\mathbf{B}$ applied to an atomic vapour separates the atomic spin states into projections onto the field axis via the Zeeman effect [Fig. 1(b)]. It is convenient to choose the quantization axis along the magnetic field, and to consider the optical and microwave polarizations with respect to this axis, in the basis of right-circular σ^+, left-circular σ^-, and parallel π polarizations. In this work with ^{87}Rb, we consider optical transitions between ground ($5S_{1/2}$) states $|g_1\rangle$ and $|g_2\rangle$ and excited ($5P_{3/2}$) states $|e_1\rangle$ and $|e_2\rangle$ that are electric-dipole allowed [blue and red arrows in Fig. 1(a, c-d)], meaning it is the oscillating electric field that defines the optical polarization. The microwave transitions we consider are within the $5S_{1/2}$ ground state manifold of the rubidium atom's structure, and are magnetic-dipole-allowed transitions between the hyperfine $|F = 1\rangle$ and $|F = 2\rangle$ levels [yellow lines in Fig. 1(b-d)], such that it is the direction of the oscillating magnetic field that defines the microwave polarization.

Next, we consider the multilevel atomic level structure shown in Fig. 1(a, c-d). When light from an optical source connects levels $|g_2\rangle$ to $|e_2\rangle$, an initial ground-state population in $|g_2\rangle$ is "pumped" to $|e_2\rangle$, at which time spontaneous emission proceeds from the excited state, and the atoms de-excite to the two available ground levels $|g_1\rangle$ and $|g_2\rangle$. If no mechanism exists for atomic population to be re-excited from $|g_1\rangle$, as in Fig. 1(a), $|g_1\rangle$ is a "dark state" and the atomic population accumulates here. A weak optical "probe" resonant from $|g_1\rangle$ to $|e_1\rangle$ will be strongly absorbed due to the large ground state population here. If, however, a microwave field connects $|g_1\rangle$ and $|g_2\rangle$ via a magnetic dipole transition, as in Fig. 1(c), atomic population will distribute between both ground states and the probe's transmission will increase as compared to the unconnected condition. Finally, we can consider the case in which the microwave field couples only one (or a subset) of the ground states, as in Fig. 1(d) (which may occur when the ground state manifold is split by an external magnetic field via the Zeeman effect), rendering the population in the connected levels empty, but the other states in that level dark, and heavily populated. By addressing particular microwave transitions via their frequencies and polarizations, we tailor the absorption medium via MAOP, and gain control over the amplitude and polarization of the light transmitted through the atomic vapour.

While controlling absorption can be effected using a resonant probe through the process just described, the polarization of the optical light can be manipulated in the dispersive regime, in which the probe is off resonance. Here, MAOP-induced atomic polarization leads to circular birefringence, due to unbalanced populations of states $|F, m_F\rangle = |1, 1\rangle$ and $|1, -1\rangle$, resulting in the rotation of the probe polarization. Assuming the single-atom refraction index is the same for each transition, the effective refractive index for each transition is proportional to the population in the corresponding level, resulting in a phase difference between the two polarization components leaving the ensemble

$$\Delta\phi = kL(n_{\sigma^+} - n_{\sigma^-}) = kLn[N_{-1} - N_{+1}], \tag{1}$$

where k is the probe wavenumber, L and the distance through which the light travels in the medium, n is the single-atom refraction index, and N_{-1} and N_{+1} are the numbers of atoms in states $|1, -1\rangle$ and $|1, 1\rangle$ states, respectively. This phase difference determines the angle by which the linear optical polarization is rotated.

3. Modelling

The model for MAOP depicted in Fig. 1 assumes a simple configuration in which the relaxation between the ground-state levels is negligible compared to the MAOP rate, so the whole atomic population accumulates in the states uncoupled from the microwave field. Our experiments are performed in a room-temperature vapour where atomic collisions with the cell walls and thermal motion through the cell region illuminated by the pump light introduce a significant relaxation between the states. In addition, due to significant Doppler broadening, several velocity classes in the atomic ensemble are resonant with different optical transitions that contribute differently to the total absorption signal observed experimentally. Here, we account for these effects, as well as experimental parameters like cavity linewidth, using a comprehensive model that treats optical pumping as a relaxation process to predict the relative optical absorption of a microwave-assisted optically pumped system of room-temperature atoms.

3.1. Hamiltonian and Lindblad equations

In our model, the Hamiltonian includes eight ground-state levels corresponding to the hyperfine- and Zeeman-split sublevels of the $5\mathrm{S}_{1/2}$ ground state of ^{87}Rb interacting with the microwave field (Fig. 2). The diagonal part of the Hamiltonian in the rotating frame (rotating at the applied microwave frequency), after applying the rotating-wave approximation, is

$$\hat{H}_0 = \hbar \sum_{m_\mathrm{F}} \left(\frac{\delta}{2} - m_\mathrm{F}\omega_\mathrm{L}\right) |F=1, m_\mathrm{F}\rangle \langle F=1, m_\mathrm{F}| + \hbar \sum_{\widetilde{m}_\mathrm{F}} \left(\widetilde{m}_\mathrm{F}\omega_\mathrm{L} - \frac{\delta}{2}\right) |F=2, \widetilde{m}_\mathrm{F}\rangle \langle F=2, \widetilde{m}_\mathrm{F}|, \tag{2}$$

where the $\omega_\mathrm{L} = \mu_\mathrm{B} B/2\hbar$ is the Larmor frequency in a static magnetic field $\mathbf{B}$ with magnitude B (already taking into account the g_F factors for ^{87}Rb's hyperfine ground states), and δ is the detuning of the microwave field from the clock ($|F=1, m_\mathrm{F}=0\rangle \rightarrow |F=2, m_\mathrm{F}=0\rangle$) transition. The interaction part is given by

$$\hat{V} = \frac{\hbar}{2} \sum_{\widetilde{m}_\mathrm{F}} \sum_{m_\mathrm{F}} \Omega_{m_\mathrm{F},\widetilde{m}_\mathrm{F}} |F=1, m_\mathrm{F}\rangle \langle F=2, \widetilde{m}_\mathrm{F}| + \mathrm{h.c.}, \tag{3}$$

where $\Omega_{m_\mathrm{F},\widetilde{m}_\mathrm{F}}$ is the Rabi frequency for coupling between between hyperfine states $|F=1, m_\mathrm{F}\rangle$ and $|F=2, \widetilde{m}_\mathrm{F}\rangle$. Note that the optical pump and probe are not included in the interaction term: the pump's optical pumping effect will be included below as an effective relaxation, while we assume the probe is very weak and does not perturb the system. If θ is the angle between the microwave magnetic field $\mathbf{B}_\mu$ and the quantizing field $\mathbf{B}$, the coupling strength for the π-transitions ($m_\mathrm{F} \rightarrow m_\mathrm{F}$) is given by [52]

$$\Omega_{m_\mathrm{F},m_\mathrm{F}} = \Omega_0 \cos\theta \sqrt{1 - g_\mathrm{F}^2 m_\mathrm{F}^2}, \tag{4}$$

where $\Omega_0 = \mu_B B_\mu/\hbar$, B_μ is the magnitude of the microwave magnetic field $\mathbf{B}_\mu$, and $g_F = 1/2$ is the Landé factor for ^{87}Rb. For the $\sigma^\pm$-transitions ($m_F \to m_F \pm 1$), the coupling strength is given by

$$\Omega_{m_F, m_F\pm 1} = \frac{\Omega_0 \sin\theta}{2I+1}\sqrt{(I \mp m_F)^2 - \frac{1}{4}}, \tag{5}$$

where $I = 3/2$ is the nuclear spin of ^{87}Rb.

The finite linewidth of the cavity is taken into account in this model by modifying the coupling strength to be dependent on detuning, and assuming this dependence has a Lorentzian character, such that

$$\Omega_{m_F,\widetilde{m}_F}(\delta) = \left(\frac{g_C^2}{g_C^2 + \delta^2}\right)\Omega_{m_F,\widetilde{m}_F}, \tag{6}$$

where g_C represents the cavity linewidth.

The dynamics of the system are described by the Lindblad master equation [53]

$$\frac{d}{dt}\hat{\rho} = -\frac{i}{\hbar}\left[\hat{H}, \hat{\rho}\right] + \frac{1}{2}\sum_n \left(2\hat{L}_n\hat{\rho}\hat{L}_n^\dagger - \hat{\rho}\hat{L}_n^\dagger\hat{L}_n - \hat{L}_n^\dagger\hat{L}_n\hat{\rho}\right), \tag{7}$$

where $\hat{\rho}$ is the density matrix, $\hat{H} = \hat{H}_0 + \hat{V}$ is the total Hamiltonian, and $\hat{L}_n$ is the collapse operator due to a relaxation process n.

We treat optical pumping, which in practice operates through an excited state level, as an effective relaxation process from ground state $|F = 2, \widetilde{m}_F\rangle$ to ground state $|F = 1, m_F\rangle$, and assign to it the collapse operator

$$\hat{L}_{OP}(m_F, \widetilde{m}_F) = \sqrt{\Gamma_{OP}}\,|F = 1, m_F\rangle\,\langle F = 2, \widetilde{m}_F|\,, \tag{8}$$

where Γ_{OP} is the optical pumping rate, which we assume is the same for all pairs of m_F and $\widetilde{m}_F$.

In the thermal equilibrium, we assume that all Zeeman sublevels of the ground-state hyperfine levels are equally occupied. This is achieved by modeling the combined thermal and wall-collision relaxation with the following collapse operator

$$\hat{L} = \sqrt{\Gamma_{th}}\,|i\rangle\,\langle j|\,, \tag{9}$$

where $|i\rangle$ and $|j\rangle$ are any two different Zeeman sublevels, and Γ_{th} is the combined thermal and wall-collision relaxation rate.

3.2. Simulating steady-state optical absorption

To model MAOP in our system, we numerically solve Eq. 7 using the computational package for Python, QuTip [54]. To begin with, we test the concept of the MAOP by looking at the populations $\rho_{m_F} = \langle F = 1, m_F|\,\hat{\rho}\,|F = 1, m_F\rangle$ in the absence of thermal and wall-collision relaxation, and with a (dimensionless) optical pumping rate

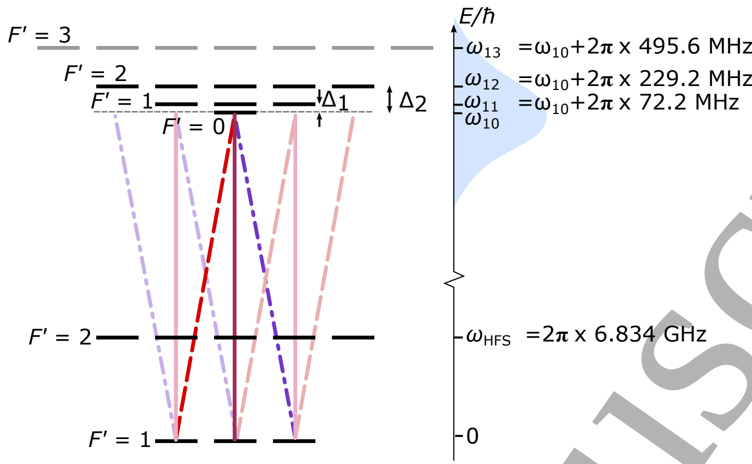

Figure 2. Level diagram for the D2 line of ^{87}Rb. The ground states in the $5S_{1/2}$ manifold are split by the hyperfine interaction into $|F=1\rangle$ and $|F=2\rangle$ levels, each of which are split into $2F+1$ Zeeman sublevels. It is between these levels that microwave transtions proceed. The excited state of interest in this work is the $5P_{3/2}$ level, and the transition between the ground state and this state is commonly known as the "D2" transition. The hyperfine interaction splits this state into four levels, denoted by "primed" labels $|F'=0,1,2,3\rangle$. The Zeeman labels are not shown, but the central sublevels denote $|m_F=0\rangle$ with positive integers to the right and negative integers to the left.
Optical transitions between the ground level $|F=1\rangle$ and the allowed excited states are denoted, with on-resonant transitions shown in dark colours and the off-resonant transitions shown more faintly. The solid lines show π-polarization transitions, while dashed lines denote σ^+-polarization transitions and dash-dot lines denote σ^-. The energies of the transtions are shown in the right vertical axis (not to scale) and the Doppler line shape is indicated (not to scale) on this axis, centered about the resonant $|F=1\rangle \to |F=0\rangle$ transitions, indicating that there is significant population for excitation by other velocity classes via the other allowed transitions.

$\Gamma_{\mathrm{OP}} = 2\pi \times 10^{-3}$, microwave Rabi frequency $\Omega_0 = 2\pi \times 10^{-5}$, and Larmor frequency $\omega_L = 4\pi \times 100$. Figure 3(a) shows the populations corresponding to the MAOP configurations π-polarized microwaves, and Fig. 3(b) with equal parts $\sigma+$ and $\sigma-$ polarizations. These simulations show that a resonant microwave field clears out the addressed sublevels, moving the atomic population to the uncoupled sublevels.

In order to simulate the optical transmission, we first need to examine how the optical absorption depends on the distribution of the atomic population between the ground-state sublevels. For a dilute vapour, the absorption is given by

$$A(\omega) = 1 - e^{-nl\sigma(\omega)} \approx nl\sigma(\omega), \tag{10}$$

where n is the atomic density, l is the length of the optical path in the medium and $\sigma(\omega)$ is the frequency-dependent absorption cross-section. For a particular $|F, m_{\mathrm{F}}\rangle \to |F', m'_{\mathrm{F}}\rangle$

transition, the cross-section is given by

$$\sigma(\omega) = A_0 N(\omega)\|d\|^2 \tag{11}$$

where A_0 is a parameter which is the same for all transitions within the D2 line, $N(\omega)$ is the fraction of atoms undergoing this transition, and $\|d\|$ is the dipole matrix element corresponding to this transition. In a thermal ensemble, due to the Doppler effect, the value of $N(\omega)$ is a product of the fraction of atoms in the velocity class resonant with the transition at frequency (ω) and the probability of an atom from this velocity class to be in the state $|F, m_\mathrm{F}\rangle$

$$N(\omega) = \sqrt{\frac{m}{2\pi k_B T}} \exp\left[-\left(\frac{c(\omega-\omega_0)}{\omega}\right)^2 \frac{m}{2k_B T}\right] \rho_{m_\mathrm{F}}, \tag{12}$$

where m is the atomic mass, T is the ensemble temperature, k_B is the Boltzmann constant, c is the speed of light, ω is the optical laser frequency, and ω_0 is the optical transition frequency in the atomic reference frame. For the D2-line, the transition matrix element given in multiples of $\langle J=1/2\|d\|J'=3/2\rangle$ is

$$\|d\| = \sqrt{S_{FF'm_\mathrm{F}m'_\mathrm{F}}}\,\langle J=1/2\|d\|J'=3/2\rangle\,, \tag{13}$$

where $S_{FF'm_\mathrm{F}m'_\mathrm{F}}$ is the relative transition strength for the transition from $|F, m_\mathrm{F}\rangle$ to $|F', m'_\mathrm{F}\rangle$.

We consider the case for which the probe is tuned to the $|F=1\rangle \to |F'=0\rangle$ transition, as shown by the darker lines in Fig. 2. Because of Doppler broadening, all three allowed transitions ($F=1 \to F'=0,1,2$) are within the Doppler linewidth (sketched as the blue curve in Fig. 2, and thus, three velocity classes contribute to the absorption: the zero-velocity atoms are resonant to the $|F=1\rangle \to |F'=0\rangle$ transition itself, which we represent by the frequency ω_{10} (through all three polarizations, darker lines), and non-zero velocity classes allows absorption through the transitions $|F=1\rangle \to |F'=1\rangle$ and $|F=1\rangle \to |F'=2\rangle$ (fainter lines in Fig. 2). Because the Doppler shift for the microwave field is negligible, the MAOP equally affects the three velocity classes. However, due to different coefficients $S_{FF'm_\mathrm{F}m'_\mathrm{F}}$ representing the different strengths of these three transitions, each velocity class contributes to the total absorption differently. To take into account the cumulative effect that the population distribution ρ_{m_F} (in the three velocity classes) has on the total absorption, we introduce a coefficient $\alpha(\omega)$, such that $A(\omega) \propto \sigma(\omega) \propto \alpha(\omega)$, with $\alpha(\omega)$ given by

$$\alpha(\omega) = \frac{1}{I}\left[I_+\alpha_+(\omega) + I_\pi\alpha_\pi(\omega) + I_-\alpha_-(\omega)\right], \tag{14}$$

where I is the total probe intensity and $I_\pm$ and I_π are intensities of the $\sigma^\pm$ and π polarization components, and

$$\alpha_+(\omega_{10}) = \sum_{m_\mathrm{F}} \rho_{m_\mathrm{F}} \sum_{F'} S_{1F'm_\mathrm{F}m_\mathrm{F}+1} \exp\left\{-\frac{m}{2k_B T}\left[\frac{c(\omega_{10}-\omega_{1F'})}{\omega_{10}}\right]^2\right\}, \tag{15}$$

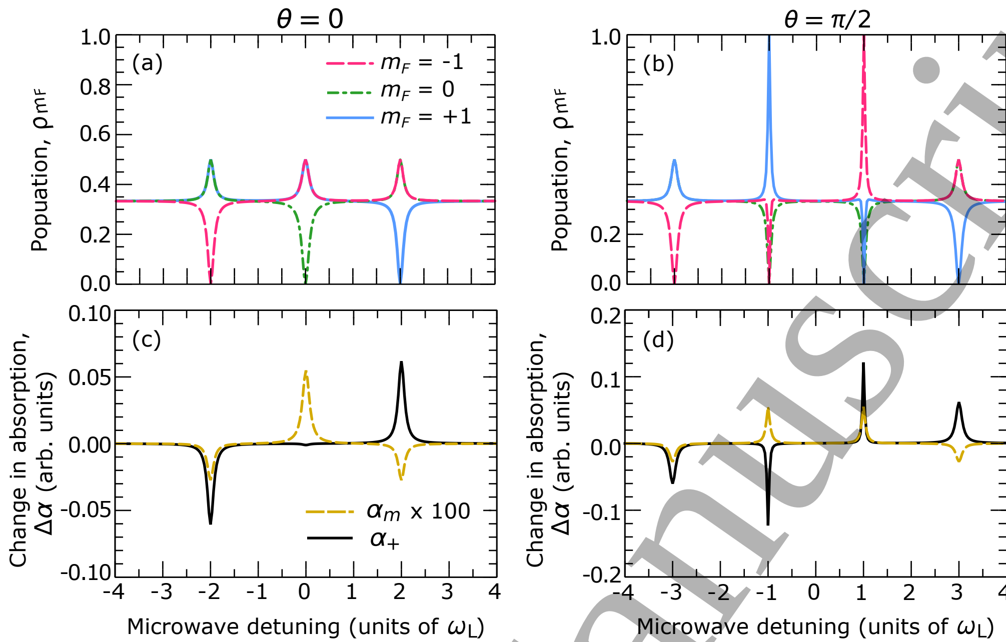

Figure 3. (a,b) Simulations of the steady-state populations of $F = 1$ sublevels under MAOP with no ground-state relaxation, and (c,d) the corresponding change in the absorption parameters α_+ and $\alpha_{\rm m}$, shown as a change from the off-resonant values, in arbitrary units. The microwave detuning δ is given with the respect to the clock transition $|F = 1, m_{\rm F} = 0\rangle \rightarrow |F = 2, m_{\rm F} = 0\rangle$. The steady state is found using the inverse-power method [55]. The simulation parameters are $\hbar = 1$, $\Gamma_{\rm OP} = 2\pi \times 10^{-3}$, $\omega_{\rm L} = 2\Gamma_{\rm OP} \times 10^5$, $\Omega_0 = \Gamma_{\rm OP} \times 10^{-2}$. (a,c) The microwave magnetic field is parallel to the quantization axis, and thus only π-polarization microwave transitions are allowed: $\theta = 0$. (b,d) The microwave magnetic field is perpendicular to the quantization axis, allowing $\sigma+$ and $\sigma-$ microwave transitions, $\theta = \pi/2$.

$$\alpha_-(\omega_{10}) = \sum_{m_{\rm F}} \rho_{m_{\rm F}} \sum_{F'} S_{1F'm_{\rm F}m_{\rm F}-1} \exp\left\{-\frac{m}{2k_BT}\left[\frac{c(\omega_{10}-\omega_{1F'})}{\omega_{10}}\right]^2\right\}, \qquad (16)$$

$$\alpha_\pi(\omega_{10}) = \sum_{m_{\rm F}} \rho_{m_{\rm F}} \sum_{F'} S_{1F'm_{\rm F}m_{\rm F}} \exp\left\{-\frac{m}{2k_BT}\left[\frac{c(\omega_{10}-\omega_{1F'})}{\omega_{10}}\right]^2\right\}, \qquad (17)$$

where $\omega_{FF'}$ is the frequency of the $|F\rangle \rightarrow |F'\rangle$ transition.

Note that off-resonant transitions from the $F = 2$ ground state are sufficiently off-resonant that we may neglect absorption from the upper level; likewise, the D1 transitions are well away from resonance and we neglect their effects.

In our MAOP configuration, the atomic population depends on the microwave detuning δ [Fig. 3(a,b)], as does, therefore, the absorption, which we now represent as $\alpha(\omega, \delta)$. Fig. 3(c,d) shows how $\alpha(\omega_{10}, \delta)$ changes due to MAOP with the microwave field detuned by δ from the clock transition. The simulation is done for two cases of probe

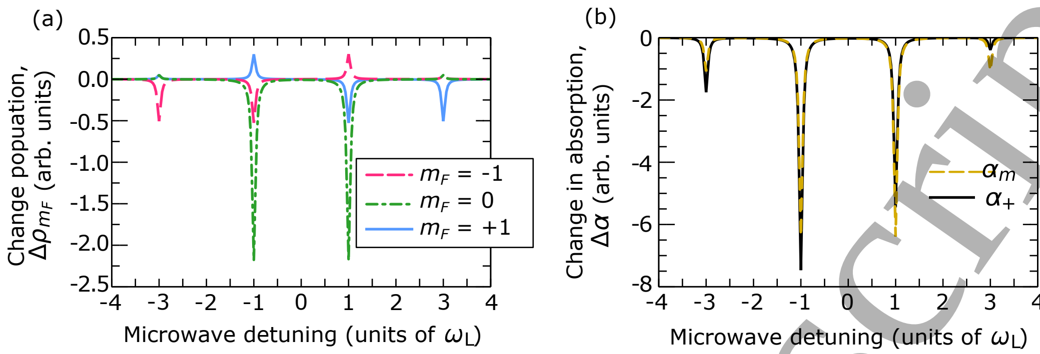

Figure 4. Simulating the change in the steady-state absorption parameter α as a function of the microwave detuning from the clock transition, taking into account the ground-state relaxation. Simulation is done with the inverse-power solution method. The simulation parameters are $\hbar = 1$, $\Gamma_{\mathrm{OP}} = 2\pi \times 10^{-3}$, $\Omega_0 = \Gamma_{\mathrm{OP}} \times 10^{-2}$, $\theta = \pi/2$, $\omega_{\mathrm{L}} = 2\Gamma_{\mathrm{OP}} \times 10^2$, $\Gamma_{\mathrm{th}} = \Gamma_{\mathrm{OP}}$, and $g_C = 0.1\omega_{\mathrm{L}}$.

polarization: first, a σ^+-polarized probe, in which case $\alpha = \alpha_+$, and second, a mixed polarization with

$$\alpha_{\mathrm{m}}(\omega,\delta) = \frac{1}{4}\alpha_+(\omega,\delta) + \frac{1}{4}\alpha_-(\omega,\delta) + \frac{1}{2}\alpha_\pi(\omega,\delta), \tag{18}$$

where half of the probe power corresponds to π-polarization and the other half is split equally between σ^+ and σ^-. As seen in [Fig. 3(c)], when there is no relaxation between the ground-state levels, MAOP should result in an antisymmetric absorption feature for a σ^+-polarized probe, and a symmetric feature for the probe with mixed polarization. In both cases, there is an increase in the absorption coefficient for some values of the microwave detuning. Next, we consider the case that includes a phenomenological term accounting for thermal and wall-collision relaxation to the simulation results, shown in Fig. 4. This realistic model is similar to what we observe experimentally, as detailed in the following section.

4. Experimental Methods

We perform experiments using a rubidium-filled vapour cell (12.5 mm × 12.5 mm × 30 mm) that is enclosed by a microwave cavity [Fig. 1(e,f)], which provides passive amplification of the microwave field and enhances magnetic dipole transitions [19, 56]. The TE_{011} cavity mode is tuned to the ground-state hyperfine transition $|F = 1, m_F = 0 \rightarrow F = 2, m_F = 0\rangle$ ($|g_2\rangle \rightarrow |g_1\rangle$) at 6.834 682 610 GHz and the microwave field power is 100 μW at the source output, chosen to enhance the effect of the microwaves without inducing power broadening. The cavity is thus resonant with the clock microwave transition (labeled "D" in Fig. 1(b)), and with a cavity linewidth of 250 kHz, all seven transitions are supported for modest external magnetic fields. The cavity linewidth effect on the transitions is included in the model in Eq. 6. The microwave cavity is a polished copper cylinder with inner diameter 58 mm and inner length of 57 mm; details on its construction can be found in Ref. [56]. The cavity has a pair of holes providing optical access for the pump and probe laser beams: for optical pumping we use the "D2" $|F=2\rangle \rightarrow |F'=2\rangle$ ($|g_2\rangle \rightarrow |e_2\rangle$) transition [Fig. 1(a)] at 780.2 nm with a laser power of $1-2$ mW. This free-running laser has a linewidth of about 100 kHz, and its polarization is set to drive linear optical transitions. The power is chosen to be just high enough to saturate the optical pumping process, and is counterpropagating to the probe so as to avoid noise from this high-power beam in the measurement. For the probe, we use powers between $10-100$ μW ensuring the probe remains well below the saturation intensity so its optical pumping rate is negligible compared to the pump beam, and set its frequency according to the particular measurement: in the absorptive regime, it is resonant with D2 $|F=1\rangle \rightarrow |F'=0\rangle$ ($|g_1\rangle \rightarrow |e_1\rangle$) transition; and in the dispersive case, the probe is significantly red-detuned from this. The transmitted probe light is measured by two Si photodectors, after passing through a polarizing beamsplitter (PBS), to determine the output beam's polarization.

By applying an external, static magnetic field $\mathbf{B}$ to the system, we lift the microwave transitions' degeneracy to give seven unique transition frequencies (Fig. 1b). In the linear Zeeman regime, identical separations between neighbouring transitions equal to $\hbar\omega_{\mathrm{L}} = \mu_{\mathrm{B}}|\mathbf{B}|/2$, where ω_{L} is the Larmor frequency, μ_{B} is the Bohr magneton and $\hbar$ is the reduced Planck constant. Typical values for the Larmor frequency are on the order of $\omega_{\mathrm{L}}/2\pi = 100$ kHz (corresponding to fields on the order of 0.1 G), which is much less than the width of the optical D2 line (on the order of MHz), meaning that both probe and pump couple to all Zeeman sublevels of a hyperfine level simultaneously. Additionally, the polarization of the microwave field is determined by the angle between the microwave magnetic field vector $\mathbf{B}_{\mu}$ (in our cavity, is along $\hat{y}$) and $\mathbf{B}$, such that we control the microwave polarization with respect to the quantization axis by rotating $\mathbf{B}$.

5. Results and Discussion

5.1. Microwave-controlled absorption

First, we study the absorptive regime in which the probe is on resonance. For these measurements, the probe is circularly polarized with respect to the propagation along $\hat{z}$, such that the unaffected output illuminates both silicon photodectors equally. Fig. 5(a,d) shows the transmission through to the photodectors as the microwave frequency varies. When $\mathbf{B} = B\hat{z}$ is parallel to the probe wavevector (Fig. 5(a-c)), the probe is σ^{+}-polarized, while the microwave field is an equal superposition of σ^{+} and σ^{-} polarizations. We see an increase in the probe transmission whenever the microwave is on resonance with an allowed microwave transition (A,C,E,G). The asymmetry in the signal in Fig. 5(a) is a consequence of MAOP creating different atomic polarizations at different frequencies, which leads to polarization filtering, as illustrated in Fig. 5(b,c). In the first case, for peak C, the microwave field simultaneously drives $|1,-1\rangle \rightarrow |2,0\rangle$ and

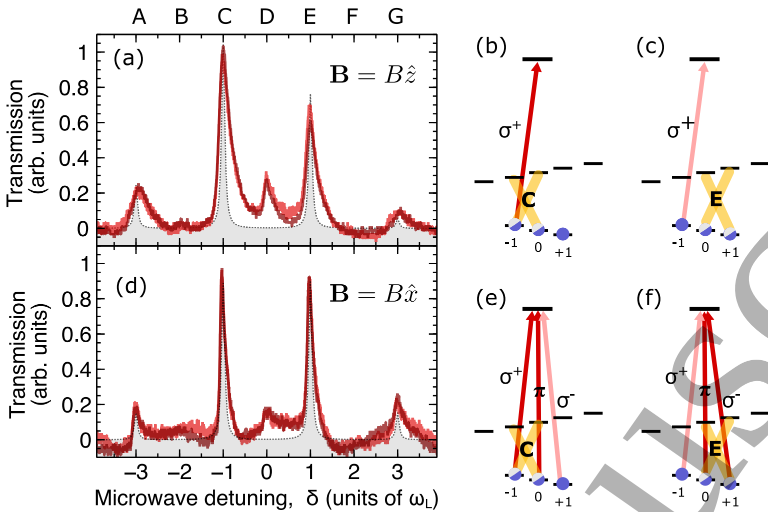

Figure 5. Microwave-controlled transmission through an atomic vapour, for $\theta = \pi/2$ ($\sigma+$ and $\sigma-$ microwave transitions). (a) Microwave-frequency dependent transmission with a σ^+-polarized optical probe across resonant Zeeman transitions (labelled A-G, as in Fig. 1); the dc magnetic field is along z. Asymmetry between resonances C (b) and E (c) is in agreement with the model (grey curve in (a)) and due to MAOP differences in ground state populations in $|F = 1, m_F = -1\rangle$ under this external magnetic field condition. (d) As in (a), but using a mixed-polarization probe that includes π and equal parts σ^+ and σ^- polarizations, because the dc magnetic field is along x. (Note that, as in (a), the optical polarization with respect to its k-vector is purely circular). Here, the transmissions are balanced between transitions C (e) and E (f), due to all three polarization components addressing all ground states in absorption. In both cases, PDs 1 and 2 give proportional readings. We use two detectors to look for a change in the probe polarization. Unlike Fig. 6, both signals overlap indicating no such change.

$|1, 0\rangle \rightarrow |2, -1\rangle$, such that MAOP transfers the atomic population to $|1, 1\rangle$. Because only the $|1, -1\rangle \rightarrow |0, 0\rangle$ transition is allowed for a σ^+ probe, its transmission is increased due to the reduced population of $|1, -1\rangle$. In the case of peak E, MAOP moves the atomic population to $|1, -1\rangle$, from which the probe can be absorbed, reducing transmission. As a check, we reversed the direction of $\mathbf{B}$, and observed a reversal of the signal's asymmetry (not shown): in this case, the probe is σ^- polarized and is absorbed more strongly when the atomic population is transferred to $|1, 1\rangle$.

Next, we performed the same measurement with the bias field $\mathbf{B} = B\hat{x}$ perpendicular to both the microwave magnetic field and the probe wave vector [Fig. 5(d-f)]. The microwave field remains $\sigma^{\pm}$ polarized, but the probe polarization now has components parallel and orthogonal to the quantization field, which couple to all three sublevels of the lower-energy ground state. Because the probe power is divided equally between σ^+ and σ^- polarization components, the atomic polarizations corresponding to opposite microwave detunings have the same effect on optical absorption, and so

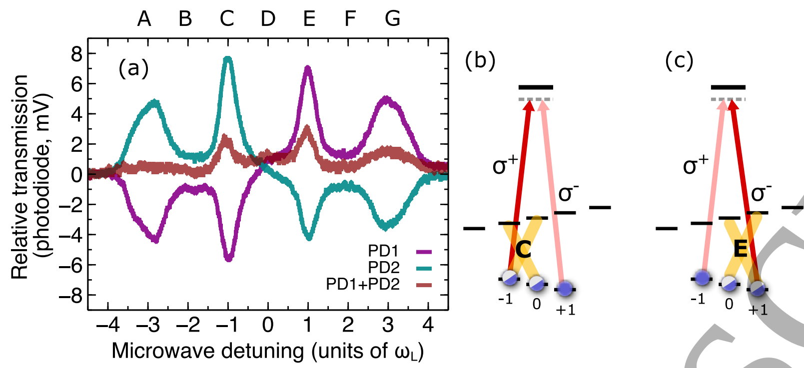

Figure 6. Microwave-controlled magneto-optical rotation. (a) Transmission detected of perpendicularly polarized input probe light (equal parts σ^+ and σ^- optical polarization) by detectors PD1 (magenta) and PD2 (cyan) (red curve is the sum). The maximum optical rotation angle corresponding to peak C is approximately 0.025 mrad. (b,c) Schematics of the microwave (yellow) and probe (red) transitions at two different microwave resonances C (b) and E (c).

the observed signal is symmetric [Fig. 5(d)]. By demonstrating atomic polarization both parallel and perpendicular to the optical pumping wavevector, we show that this approach enables versatile control over the atomic polarization at and between these orthogonal conditions, through the choice of magnetic field at or between these limiting cases.

To fully explain the signals observed in Fig. 5(a,d), we compare our results to the theoretical model describing MAOP discussed in the previous section, which includes the additional contribution to the absorption from the velocity classes resonant with $|F=1\rangle, \rightarrow |F'=1\rangle$ and $|F=1\rangle \rightarrow |F'=2\rangle$ transitions, which are accessible due to the Doppler effect. Fig. 5(a,d) (grey shaded area) shows the transmission coefficient calculated for an ensemble dominated by thermal relaxation between the ground-state levels (using the same parameters as in Fig. 4: (dimensionless) optical pumping rate $\Gamma_{\mathrm{OP}} = \Gamma_{\mathrm{th}} = 2\pi \times 10^{-3}$, microwave Rabi frequency $\Omega_0 = 2\pi \times 10^{-5}$, and Larmor frequency $\omega_L = 4\pi \times 100$), and it is in a good agreement with the observed signal. While in our model, we assume that the microwave magnetic field is perfectly aligned with the cavity axis, the microwave field orientation varies in space and is not fully aligned with the cavity axis outside the cavity center. Since our cell occupies a finite area inside the cavity, some atoms experience microwave fields not orthogonal to the DC field, and, in addition, if the probe is not perfectly perpendicular to the cavity axis, this effect is even stronger. Since the central peak corresponds to the strongest microwave transition, some signal is measured here due to these artifacts.

5.2. Microwave-controlled magneto-optical rotation

Second, we explore effects in the dispersive regime in which the probe is below resonance. To observe this optical rotation, a linearly polarized probe whose frequency is set to the lower-frequency edge of the Doppler-broadened absorption peak of the D2-line originating in the $F = 1$ level is sent through the atoms. The probe is red-detuned from the $|F = 1\rangle \rightarrow |F' = 0\rangle$ transition to the extent where its absorption is reduced and the dispersion is enhanced compared to the resonant case. With a half-wave plate, we set the probe polarization at 45° with respect to the x-axis ($-45°$ with respect to the y-axis), which in the case of no atom-mediated rotation, splits the probe power equally between the two photodetectors through the PBS. Any optical rotation through the medium thus results in opposite changes measured by the two detectors, without affecting the total optical power. The external magnetic field is applied parallel to the probe, so the perpendicular-linear probe polarization is an equal superposition of σ^+- and σ^--polarizations.

Fig. 6(a) shows the relative transmission measured by D1 and D2 across a linear sweep of the microwave frequency. When the microwave field is on resonance with an allowed hyperfine transition, transmission is increased on one photodetector while decreasing on the other, indicating optical rotation. A small degree of absorption renders the sum of the two transmissions to be small but not exactly zero. Transmission as a function of frequency is antisymmetric with respect to the clock-transition frequency (resonance D), indicating that the polarization rotation depends on the sign of the microwave detuning. As seen in Eq. 1, this is a consequence of a change in the sign of the population difference between levels $|1, 1\rangle$ and $|1, -1\rangle$, and thus a change in the "direction" of the atomic polarization [Fig. 6(b,c)] If we turn off the pump light or set its frequency off-resonance, the observed signal feature disappears, which suggests that the observed circular birefringence of the vapour results from MAOP and not from the non-linear interaction between the microwave field and the probe itself. We also highlight that when the microwave field is not on resonance with any transition, no optical rotation is observed.

In this work, the optical rotation due to polarization of atomic vapour discussed above corresponds to *paramagnetic* Faraday rotation [57], which differs from diamagnetic Faraday rotation, where the optical rotation angle is proportional to the magnitude of a strong static magnetic field applied parallel to the optical beam [58]. In the case of diamagnetic Faraday rotation, transitions corresponding to different circular polarizations experience different frequency shifts due to the interaction with the static magnetic field leading to the circular birefringence. In our case, the optical rotation is determined by the microwave parameters, which allows for microwave control of optical polarization.

6. Conclusion

In this work, we have shown through theoretical modelling and experimental demonstrations that optical dichroism and circular birefringence can be controlled by microwave fields through microwave-assisted optical pumping in a thermal atomic vapour, with arbirtary atomic polarization enabled by modifying an external magnetic field orientation rather than redirecting optical beams. By demonstrating a suite of techniques in the domain of microwave-to-optical control [3], this approach offers possibilities for a microwave-controlled polarization-selective optical filter or switch that could encode polarization states of light, where applying a microwave field makes the atomic vapour transparent for light with a particular polarization, rotates its polarization, with applications to microwave-to-optical transduction, or for quantum state engineering for quantum information [59]. While the current platform of thermal atoms offers opportunities for low-cost technologies, we expect more prominent performance in cold ensembles, where collisional and spin-exchange relaxation between the ground-state levels are reduced.

Acknowledgements

We thank Andal Narayanan for helpful discussions and useful feedback on this manuscript. This work was supported by the University of Alberta; the Natural Sciences and Engineering Research Council, Canada (Grants No. RGPIN-04523-16, No. RGPIN-2021-02884, and No. CREATE-495446-17); the Alberta Quantum Major Innovation Fund; Alberta Innovates; and the Canada Research Chairs (CRC) Program. As researchers at the University of Alberta, we acknowledge that we are located on Treaty 6 territory, and that we respect the histories, languages, and cultures of First Nations, Métis, Inuit, and all First Peoples of Canada, whose presence continues to enrich our vibrant community.

References

[1] Georgescu I M, Ashhab S and Nori F 2014 *Reviews of Modern Physics* **86** 153–185
[2] Ludlow A D, Boyd M M, Ye J, Peik E and Schmidt P O 2015 *Reviews of Modern Physics* **87** 637–701
[3] Lauk N, Sinclair N, Barzanjeh S, Covey J P, Saffman M, Spiropulu M and Simon C 2020 *Quantum Science and Technology* **5** 020501
[4] Vewinger F, Appel J, Figueroa E and Lvovsky A I 2007 *Optics Letters* **32** 2771
[5] Gard B T, Jacobs K, McDermott R and Saffman M 2017 *Physical Review A* **96** 013833
[6] Han J, Vogt T, Gross C, Jaksch D, Kiffner M and Li W 2018 *Physical Review Letters* **120** 093201
[7] Vogt T, Gross C, Han J, Pal S B, Lam M, Kiffner M and Li W 2019 *Physical Review A* **99** 023832
[8] Liang Z T, Lv Q X, Zhang S C, Wu W T, Du Y X, Yan H and Zhu S L 2019 *Chinese Physics Letters* **36** 080301
[9] Liu Y G, Xia K and Zhu S L 2021 *Optics Express* **29** 9942
[10] Cox K C, Meyer D H, Fatemi F K and Kunz P D 2018 *Physical Review Letters* **121** 110502
[11] Deb A B and Kjærgaard N 2018 *Applied Physics Letters* **112** 211106
[12] Anderson D A, Sapiro R E and Raithel G 2021 *IEEE Transactions on Antennas and Propagation* **69** 2455–2462

[13] Meyer D H, Cox K C, Fatemi F K and Kunz P D 2018 *Applied Physics Letters* **112** 211108
[14] Song Z, Liu H, Liu X, Zhang W, Zou H, Zhang J and Qu J 2019 *Optics Express* **27** 8848
[15] Jiao Y, Han X, Fan J, Raithel G, Zhao J and Jia S 2019 *Applied Physics Express* **12** 126002
[16] Gordon J A, Simons M T, Haddab A H and Holloway C L 2019 *AIP Advances* **9** 045030
[17] Simons M T, Haddab A H, Gordon J A and Holloway C L 2019 *Applied Physics Letters* **114** 114101
[18] Holloway C L, Simons M T, Haddab A H, Williams C J and Holloway M W 2019 *AIP Advances* **9** 065110
[19] Tretiakov A, Potts C A, Lee T S, Thiessen M J, Davis J P and Leblanc L J 2020 *Applied Physics Letters* **116** 164101
[20] Li C, Sun F, Liu J, Li X, Hou D and Zhang S 2021 *Applied Physics Letters* **119** 154001
[21] Lvovsky A I, Sanders B C and Tittel W 2009 *Nature Photonics* **3** 706–714
[22] Zhang R, Garner S R and Hau L V 2009 *Physical Review Letters* **103** 233602
[23] Katz O and Firstenberg O 2018 *Nature Communications* **9** 2074
[24] Saglamyurek E, Hrushevskyi T, Rastogi A, Cooke L W, Smith B D and LeBlanc L J 2021 *New Journal of Physics* **23** 043028
[25] Pétremand Y, Affolderbach C, Straessle R, Pellaton M, Briand D, Mileti G and De Rooij N F 2012 *Journal of Micromechanics and Microengineering* **22** 25013
[26] Pellaton M, Affolderbach C, Pétremand Y, De Rooij N and Mileti G 2012 *Physica Scripta* **T149** 14013
[27] Stefanucci C, Bandi T, Merli F, Pellaton M, Affolderbach C, Mileti G and Skrivervik A K 2012 *Rev. Sci. Instrum.* **83** 104706
[28] Bandi T, Affolderbach C, Stefanucci C, Merli F, Skrivervik A K and Mileti G 2014 *IEEE Transactions on Ultrasonics, Ferroelectrics, and Frequency Control* **61** 1769–1778
[29] Guo Y, Wang S, Zhu L, Cai Z, Lu F, Li W and Liu Z 2023 *Rev. Sci. Instrum.* **94** 014706
[30] Sedlacek J A, Schwettmann A, Kübler H and Shaffer J P 2013 *Physical Review Letters* **111** 063001
[31] Kinoshita M, Shimaoka K and Shimada Y 2013 *IEEE Transactions on Instrumentation and Measurement* **62** 1807–1813
[32] Sun F, Ma J, Bai Q, Huang X, Gao B and Hou D 2017 *Applied Physics Letters* **111** 051103
[33] Shi H, Ma J, Li X, Liu J, Li C and Zhang S 2018 *Sensors* **18** 3288
[34] Liu X, Jiang Z, Qu J, Hou D, Huang X and Sun F 2018 *Review of Scientific Instruments* **89** 063104
[35] Tretiakov A and Leblanc L J 2019 *Physical Review A* **99** 43402
[36] Kominis I K, Kornack T W, Allred J C and Romalis M V 2003 *Nature* **422** 596–599
[37] Ben-Kish A and Romalis M V 2010 *Physical Review Letters* **105** 193601
[38] Patton B, Zhivun E, Hovde D C and Budker D 2014 *Physical Review Letters* **113** 13001
[39] Limes M E, Foley E L, Kornack T W, Caliga S, McBride S, Braun A, Lee W, Lucivero V G and Romalis M V 2020 *Physical Review Applied* **14** 11002
[40] Zhang R, Xiao W, Ding Y, Feng Y, Peng X, Shen L, Sun C, Wu T, Wu Y, Yang Y, Zheng Z, Zhang X, Chen J and Guo H 2020 *Science Advances* **6** 8792–8804
[41] Walker T G and Happer W 1997 *Reviews of Modern Physics* **69** 629–642
[42] Vasilakis G, Brown J M, Kornack T W and Romalis M V 2009 *Physical Review Letters* **103** 261801
[43] Kitching J, Knappe S and Donley E A 2011 *IEEE Sensors Journal* **11** 1749–1758
[44] Horsley A, Du G X and Treutlein P 2015 *New Journal of Physics* **17** 112002
[45] Pedreros Bustos F, Bonaccini Calia D, Budker D, Centrone M, Hellemeier J, Hickson P, Holzlöhner R and Rochester S 2018 *Nature Communications* **9** 3981
[46] Katz O and Firstenberg O 2019 *Communications Physics* **2** 58
[47] Wineland D J, Bergquist J C, Itano W M and Drullinger R E 1980 *Optics Letters* **5** 245
[48] Demtröder W 1996 Optical Pumping and Double-Resonance Techniques *Laser Spectroscopy: Basic Concepts and Instrumentation* (Berlin, Heidelberg: Springer Berlin Heidelberg) pp 552–593 ISBN 978-3-662-08260-7 URL `https://doi.org/10.1007/978-3-662-08260-7_10`
[49] Sarreshtedari F, Rashedi A, Ghashghaei F and Sabooni M 2021 *Physica Scripta* **96**

[50] Zigdon T, Wilson-Gordon A D, Guttikonda S, Bahr E J, Neitzke O, Rochester S M and Budker D 2010 *Optics Express* **18** 25494

[51] Fenwick K L, England D G, Bustard P J, Fraser J M and Sussman B J 2020 *Optics Express* **28** 24845

[52] This equation and the next are derived using the Wigner-Eckhart theorem and explicit expressions for the Clebsch-Gordon coefficients, which can be found in several reference texts including: Brink D M and Satchler G R (2015) *Angular Momentum, 3rd ed.* (Oxford: Clarendon Press)

[53] Auzinsh M, Budker D and Rochester S M 2010 *Optically Polarized Atoms: Understanding Light-atom Interactions* (Oxford: Oxford University Press)

[54] Johansson J R, Nation P D and Nori F 2013 *Computer Physics Communications* **184** 1234–1240

[55] Nation P D 2015 *arxiv.org* 1504.06768

[56] Ruether M, Potts C A, Davis J P and LeBlanc L J 2021 *Journal of Physics Communications* **5** 121001

[57] Takeuchi M, Takano T, Ichihara S, Takasu Y, Kumakura M, Yabuzaki T and Takahashi Y 2006 *Applied Physics B* **83** 107–114

[58] Siddons P, Adams C S and Hughes I G 2010 *Physical Review A* **81** 043838

[59] An F A, Ransford A, Schaffer A, Sletten L R, Gaebler J, Hostetter J and Vittorini G 2022 *Phys. Rev. Lett.* **129**(13) 130501